Applied Physics A (2022) 128:337
https://doi.org/10.1007/s00339-022-05295-5

Applied Physics A
Materials Science & Processing

Analysis of the photocurrent from CuO/TiO_2 nanostructured photoelectrodes to elucidate the benefits of nanocrystal size decrease

Fresnel Forcade[1] · Bernardo González[1] · Rony Snyders[2,3] · Xavier Noirfalise[2] · Elena Vigil[1,4]

Received: 29 September 2021 / Accepted: 2 January 2022 / Published online: 24 March 2022

Abstract

CuO/TiO_2 nanostructured photoelectrodes obtained with a modified immersion technique are analyzed, and their photocurrents are compared in order to study the effect of nanocrystals size decrease; which leads to a favorable conduction bands alignment. For this purpose, very small precursor concentration and immersion times are selected for CuO/TiO_2 film fabrication. This affects the amount of CuO deposited inside the TiO_2 mesoporous film and decreases the number of absorbed photons, as well as, the number of generated electron–hole pairs. Calculations account for these effects. When CuO nanocrystals size is reduced, CuO/TiO_2 energy bands alignment improves electron injection from CuO to TiO_2 but internal surfaces and defects acting as traps increase. This study considers the interplay of these phenomena. Results indicate that it is beneficial to reduce nanocrystal size in spite of internal surface recombinations.

Keywords CuO/TiO_2 · PEC photoelectrode · Photocurrent · Nanocrystal size · Band engineering

1 Introduction

The CuO/TiO_2 three-dimensional interface has recently been reported for solar cell applications [1–8]; a maximum efficiency of 2.14% was achieved [3]. This interface has been studied also for water splitting to generate hydrogen. For this purpose, several ways of combining CuO and TiO_2 have been used in suspended-particle systems [9–13], as well as in photoelectrodes for photoelectrochemical cells (PEC) [12, 14–19]. Agreement exists regarding the essential role of light absorption by CuO in improving water splitting when added to TiO_2 [12, 15, 18–20]. CuO absorbs photons in a wider range of the visible spectrum which TiO_2 cannot absorb because of its higher energy gap, E_g (for anatase $E_g = 3.2$ eV (388 nm) while for rutile $E_g = 3.0$ eV (413 nm) [21]). CuO is a p-type semiconductor [22] which presents a bandgap value in the range $1.2 \leq Eg \leq 1.5$ eV [23–34]. This value depends on nanocrystal size and morphology [22], and even higher values have been reported [35].

Previouosly mentioned research papers point to the existing interest and importance of the CuO/TiO_2 interface. The modified immersion technique is an economical and scalable route to fabricate PEC photoelectrodes with the possibility of controlling nanocrystal size, as previously reported [36]. Smaller CuO nanocrystals deposit inside TiO_2 nanopores when the precursor solution concentration and the immersion time decrease [36]; therefore, very short immersion times and a low precursor solution concentration are used for this study.

By reducing the nanocrystal size, the relative position of the CuO and TiO_2 conduction bands should move to favor electron injection from CuO to TiO_2 but a smaller amount of CuO is deposited inside the TiO_2 mesoporous film with this technology. This leads to a decrease in the number of absorbed photons, as well as, in the number of generated electron–hole pairs; calculations performed account for these effects. A larger number of recombination at different interfaces occurs for an increase in the number of smaller nanocrystals but equal CuO mass. Therefore, benefits of band engineering from nanocrystal size reduction could be absent. To elucidate whether crystal size reduction is beneficial, photocurrent values are analyzed and compared.

✉ Elena Vigil
evigil@fisica.uh.cu

1 Materials Science and Technology Institute, Havana University, Havana, Cuba

2 Materia Nova Research Center, Mons, Belgium

3 Center of Innovation and Research in Materials and Polymers, University of Mons, Mons, Belgium

4 Physics Faculty, Havana University, Havana, Cuba

2 The CuO/TiO_2 nanocrystalline interface

2.1 Processes taking place in the CuO/TiO_2 photoelectrode

Figure 1 shows the main processes taking place in a photoelectrode made of a CuO/TiO_2 nanocrystalline composite with a three dimensional interface. White thick arrows indicate processes that contribute positively to photocurrent while black arrows represent undesirable recombination mechanisms. The η_{ABS} arrow identifies photon absorption and creation of electron–hole pairs, while the η_{INJ} one corresponds to electron injection from the CB of the CuO to that of TiO_2. The η_{TRAN} arrow indicates electron transport in the TiO_2. The η_{COL} one identifies charge collection in the TiO_2/FTO interface. The E arrow corresponds to electron transfer from an electrolyte (or other hole conductor) to the CuO. ST1 represents surface states and traps at the CuO/TiO_2 interface. ST2 represents surface states and traps at the TiO_2/TiO_2 interface. Finally, ST3 represents defect states and traps in the TiO_2/FTO interface. The photocurrent of a PEC depends on all of these processes.

2.2 Recombination losses inside the nanoparticle

Electron–hole recombination inside the nanoparticles (process 1 in Fig. 1) must be avoided for solar radiation converting devices. Assuming spherical nanocrystals with radius R and that excited electron–hole pairs created by photons move randomly, Hagfeldt and Graetzel [37] report that recombination time τ_d is given by:

$$\tau_d = \frac{R^2}{\pi^2 D} \tag{1}$$

where D is the material diffusion coefficient. Equation (1) implies that electron–hole recombination of excited carriers inside the nanoparticle can be prevented decreasing nanocrystal size.

2.3 Charge separation in the TiO_2/CuO interface

Band bending exists for bulk heterojunctions due to charge distribution. Electron–hole pairs are separated by the electric field at the depletion region which corresponds to a potential difference Δφ. In this case, at equilibrium, Fermi levels align themselves, and doping concentrations contribute to determine the difference between bands of each semiconductor [38, 39]. But nanocrystal size affects band alignment in nanocrystalline heterostructures. Curran and Lamouche [40] estimated the minimum value of the potential difference Δφ capable to separate charges. It is given by the relation $2kT/q$ that takes an approximate value of 52 mV for room temperature ($T = 27\ ^\circ C = 300$ K). Accordingly, Peter [39] reports that if the potential difference Δφ is smaller than kT/q, it has a negligible effect on the charge distribution; i.e., a depletion region would not exist.

For semiconducting spherical nanoparticles of radius R, the potential difference between the surface and the center of the nanoparticle is given by [41, 42]:

$$\Delta\varphi = \frac{kT}{6q}\left(\frac{R}{L_D}\right)^2 \tag{2}$$

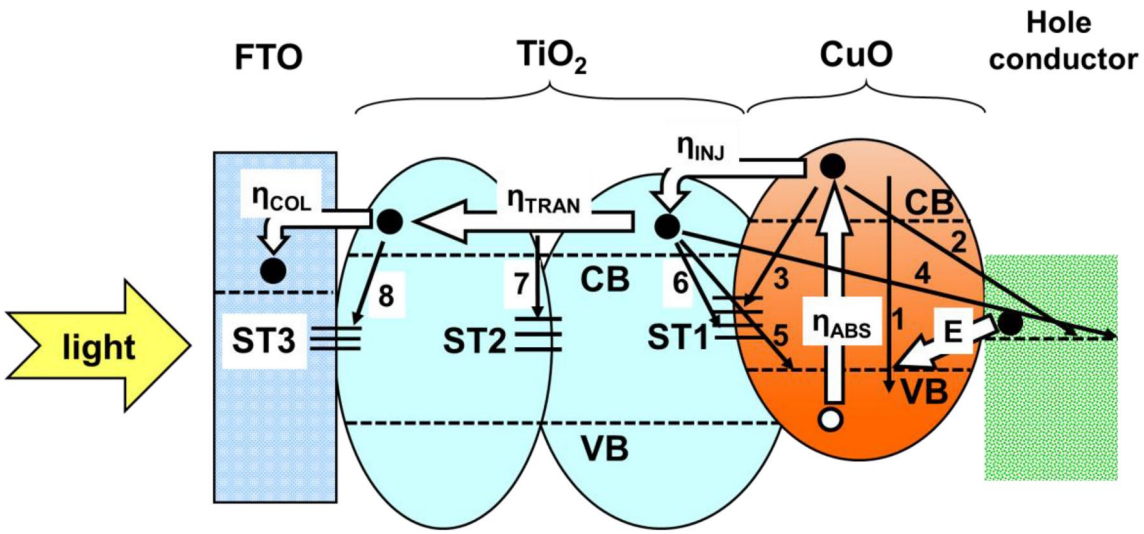

Fig. 1 Processes taking place in the CuO/TiO_2 photoelectrode. The black circle represents electrons, while the white one represents holes. White thick arrows indicate processes that contribute positively to photocurrent and undesirable recombination processes are represented by black arrows. CB and VB indicate the conduction and valence bands, respectively

where L_D is the Debye length, and q is the electron charge. The Debye length L_D is given by [42]:

$$L_D = \left(\frac{\epsilon_0 \epsilon kT}{q^2 N_I}\right)^{1/2} \quad (3)$$

where ϵ_0 is the vacuum permittivity, ϵ the static dielectric constant of the material, and N_I is the impurity concentration (donors or acceptors).

In the case of TiO_2 Degussa P25, using expressions (2) and (3), $L_D \approx 12$ nm and $\Delta\varphi \approx 5$ mV for $\varepsilon_{TiO_2} \approx 100$, [43, 44], $N_I = 10^{24}$ m^{-3} [45], $R = 12.5$ nm [46] and $T = 300$ K. Therefore, the existing small electric field cannot separate charge carriers in the case of TiO_2 Degussa P25 with close to round particles of 15–25 nm diameter [46].

According to expressions (2) and (3), $L_D \approx 15$ nm and $\Delta\varphi \approx 4$ mV for a CuO spherical nanoparticle of radius $R = 15$ nm [36], relative dielectric constant $\epsilon_{CuO} = 12.3$ [47] and concentration of acceptor impurities $N_{Ai} = 7.5 \bullet 10^{22}$ m^{-3} [48]. Therefore, in the case of CuO nanoparticles with 30-nm-diameter or less, charges will not be separated by an electric field at the interface because $\Delta\varphi < kT/q$. When the potential drop cannot separate electron–hole pairs, band positions relative to vacuum of each semiconductor will determine thermodynamic charge transfer; which depends on the energy difference ΔE between the conduction bands in the case of the analyzed CuO/TiO_2 interface. Therefore, when CuO nanocrystal size decreases and the gap increases, its conduction band should move to higher energies [49, 50], and electron transfer probability from CuO to TiO_2 should improve.

3 Experimental description

In order to decrease CuO nanocrystal size and increase bandgap and ΔE values, CuO/TiO_2 composite films are fabricated on conducting glass with the previously reported modified immersion technique [51]. Smaller CuO nanocrystals deposit inside TiO_2 nanopores when the precursor solution concentration and the immersion time decrease [36]; therefore, very short immersion times and a low precursor solution concentration are used for this study. Films are employed as PEC photoelectrodes, and photocurrents are analyzed in order to study competing phenomena.

3.1 Mesoporous TiO_2

Pieces of fluor-doped tin oxide glass (FTO TEC-15, sheet resistance 15 Ω/square) were cleaned ultrasonically with 2-propanol and then with distilled water (during 3 min each). A TiO_2 blocking film was grown on the FTO glass by microwave activated chemical bath deposition (MW-CBD) [52, 53]. For this purpose, equal volumes of 3.4×10^{-2} M ammonium hexafluorotitanate aqueous solution and 6.8×10^{-2} M boric acid aqueous solution were mixed to form the precursor used [52, 53]. The substrate was introduced vertically in this precursor solution at the center of a microwave oven model MS-71 M. Microwave radiation was applied during 15 s at 660 W.

A single layer of mesoporous TiO_2 was deposited on top of the TiO_2 blocking films using TiO_2 nano-powder (P25 Titanium dioxide, Degussa AG, Germany) with the well-known "doctor blade" technique developed for DSSC [51]. Also, mesoporous TiO_2 was deposited on bare optical-glass substrates for some analysis. The final area of all TiO_2 films was limited to 10×10 mm^2. Air drying of the TiO_2 layer was followed by heat treatment in air for an hour at 450 °C in order to produce the so-called necking between nanocrystals.

3.2 Fabrication of CuO/TiO_2 composite

In order to obtain the CuO/TiO_2 interface, the porous TiO_2 films were immersed in a 40 mM Cu (II) formate ($Cu(HCOO)_2$) aqueous solution [51]; solution was prepared with Cu (II) formate hydrate, 97% (Sigma-Aldrich). Immersion time used were 10 min, 1 min and 30 s to decrease CuO nanocrystal size [36], and sample types were named 40F_10min, 40F_1min and 40F_30s, respectively. During immersion, Cu (II) formate adheres to the TiO_2; precursor molecules should move easily through the mesoporous structure and penetrate pores according to their relative dimensions [51]. After immersion, the samples were heat treated in air for three hour at 500 °C. In this process, water evaporates, adhered Cu (II) formate decomposes to CuO inside TiO_2 pores and a CuO/TiO_2 interface is formed [51].

3.3 Characterization of CuO/TiO_2 films

Film thickness was measured by means of a Dektak 150 profilometer. This device scans a certain length of the sample showing thickness behavior. It gives the mean surface roughness (defined as the arithmetic average of the absolute value of the deviations of the thicknesses relative to their mean). Measurements were taken in three different zones, and the thickness and roughness values were given by the average values of the three scan. This surface roughness value is considered the uncertainty in the thickness. The CuO/TiO_2 morphology was evaluated by scanning-electron microscopy (SEM) using a Hitachi SU8020 scanning electron microscope. For phase identification of the films, an Empyrean Panalytical X-ray diffraction apparatus was used. Cu Kα radiation ($\lambda = 1.5406$ Å) was employed for all X-ray diffraction experiments performed in the range $10° < 2\theta < 60°$. A grazing angle equal to 0.5° was used for all samples. The Panalytical software for XRD, HighScore version 3.0

(2012), served for XRD pattern analysis. A double beam UV–VIS-NIR Cary 5G spectrophotometer was used for optical transmittance and total reflectance spectra of the films (range 300–1300 nm).

3.4 PEC cell photocurrent measurements

To evaluate photocurrent behavior of CuO/TiO_2 photoelectrodes, a two-electrode photoelectrochemical cell (PEC) with dimensions $2.5 \times 3.3 \times 4.0$ cm^3 is used [54]. The photoelectrodes are made by depositing silver paint on the upper part of the FTO glass (not covered by the CuO/TiO_2 nor by the TiO_2 blocking film) to allow the connection of a thin wire. A platinum counter electrode is utilized. A pH 6 solution of water and ethanol (1/30 v/v, 0.4 ml of alcohol in 12 ml of distilled water) is employed as electrolyte. Filtered light from a 50 W halogen lamp illuminates the photoelectrode. An orange filter only transmits wavelengths higher than 520 nm (i.e., photon energies smaller than 2.38 eV) to avoid light absorption by the TiO_2. A 200 mW/cm^2 light intensity on the photoelectrode is achieved with focusing lenses and measured with a calibrated photodiode. The PEC cells are placed inside a Faraday box that additionally avoids possible room illumination. An Agilent 34410A multimeter acts as nanoamperimeter; it is connected to a personal computer in order to control measurements and collect data. Photocurrent behavior for light on and off cycles is recorded without any applied voltage.

4 Results and discussion

After heat treatment the samples color changed from a pale bluish tint to a pale brownish one, indicating that the adsorbed Cu (II) formate decomposes to CuO as expected.

4.1 Structural and morphological analysis

Figure 2 shows SEM images of typical surfaces of samples 40F_10min and 40F_30s which reveal a nanostructured morphology.

All particles look alike for both samples in Fig. 2. Neither size nor morphology differences distinguish CuO and TiO_2 particles. No CuO particles larger than TiO_2 are visible confirming CuO growth inside TiO_2 pores. This is important to neglect recombination within the CuO nanocrystal since CuO reported diffusion length for holes is $L_D = 40$ nm [48].

Figure 2 also shows that visible pores allow penetration by an electrolyte or other media required by some devices based on the CuO/TiO_2 interface.

XRD pattern for sample 40F_10min in Fig. 3a, shows only anatase and rutile peaks; in spite that CuO concentration is the highest since a longer immersion time increases the CuO concentration [36]. This indicates that CuO concentration is below the XRD equipment sensitivity even for this sample with CuO concentration higher than for the other two sample types. Accordingly, only anatase and rutile peaks showed in XRD of samples 40F_1min and 40F_30s. Previous work showed that X-ray peak-intensity of CuO increases with precursor concentration [51] or longer immersion time [36]. In order to confirm why CuO diffraction peaks are not visible for samples studied here, two samples, 160F_1h and 160F_1min, were prepared and analyzed using XRD. They were obtained as described before but the precursor solution concentration was bigger, 160 mM, and immersion times were one hour and one minute. Figure 3b for samples 160F_1h and 160F_1min shows that CuO peaks are hardly visible for 1 min immersion time. It is understandable that CuO peaks would not show for the smaller concentration (40 mM instead of 160 mM) and immersion times used here; in spite that, color changes

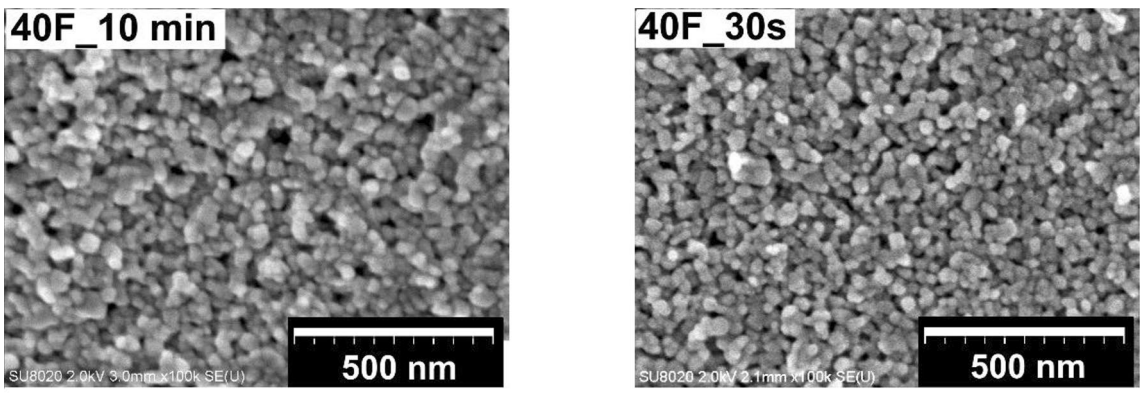

Fig. 2 SEM images of samples surface **a** 10 min immersion time **b** 30 s immersion time

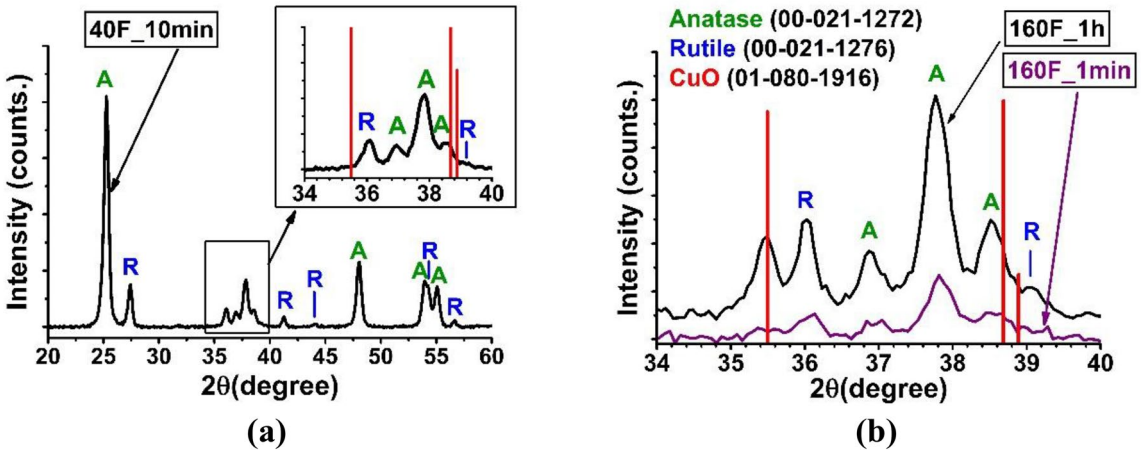

Fig. 3 **a** XRD pattern of sample 40F_10min deposited on optical-glass substrates (reference code for anatase and rutile [55]). Inserted, a zoom of the 34°-40° range (vertical lines according to reference code for CuO [56]). **b** XRD pattern of samples 160F_1h and 160F_1min used for comparison. The letters A and R identify the anatase and rutile phases, respectively, while the vertical lines identify CuO pattern

of the samples from white to bluish to brownish were visible during the technological procedure.

4.2 Photoelectrodes characterization

Figure 4 shows the time dependence of the short circuit photocurrent for the three types of photoelectrodes illuminated with filtered light to avoid electron–hole pairs created in the TiO_2. This decreases efficiency not only because part of the light spectrum is cut-off but also because CuO absorption of photons with higher-than-bandgap energy increases as the wavelength decreases. Besides, TiO_2 photoconductivity most probably decreases. Nonetheless, it is needed to analyze the effect of nanocrystal size decrease. The sense of all measured photocurrents corroborates the fact that the CuO sensitizes the TiO_2, i.e., electrons are injected from the CuO to the TiO_2. Both, the hardly possible electron injection from TiO_2 to CuO or the possible CuO contact (p-type) with the FTO, would produce a current in the opposite sense. Existing photocurrent sense indicates a positive value of ΔE, i.e., values of CuO occupied levels in its conduction band are higher than some empty ones in TiO_2 conduction band.

Considering photocurrent behavior in PECs, the same initial cycle is considered for all samples. Also, photocurrent density, J_{LIGHT}, is given by:

$$J_{LIGHT} = J_{MAX} - J_{DARK} \tag{4}$$

where J_{DARK} corresponds to the initial dark current, and J_{MAX} is the maximum value reached when light is turned on. It should be noted that wavelengths λ smaller than 520 nm are filtered out and do not contribute to photocurrent. This decreases the short circuit photocurrent, as explained before, and it determines the reported photocurrent values.

Figure 4b shows that J_{LIGHT} values decrease for shorter immersion times. Apparently, results do not improve for lower immersion times for which nanocrystal size are smaller. But, one has to take into account that light absorption decreases for shorter immersion times because smaller quantities of CuO deposite inside the TiO_2 [36]. Therefore, in the next Sects. 4.3 and 4.4, photocurrents are compared as if light absorption were equal.

4.3 Optical absorption by CuO

Light absorption depends on the CuO concentration that is different for each sample. If the CuO absorption coefficient, α_{CuO}, is known, the following relation can be applied in the spectral zone where neither the TiO_2 nor the FTO absorb:

$$\frac{I_T}{I_i} = \frac{I_T}{I_0(1-R)} = \exp\left(-\alpha_{com} t_{com}\right) = \exp\left(-\alpha_{CuO} t_{eq}\right) \tag{5}$$

where I_T, is the transmitted light intensity, I_i is the incident light intensity given by $I_i = I_0(1-R)$ since part of the total intensity I_0 is reflected. α_{com} is the absorption coefficient for each CuO/TiO_2 film, t_{com} is the actual composite film thickness, and t_{eq} is an equivalent CuO thickness that would absorb as much light as the CuO distributed inside the TiO_2. Figure 5 illustrates this assumption (scale and proportions are exaggerated). For the spectral zone where neither the TiO_2 nor the FTO absorb, expression (5) yields:

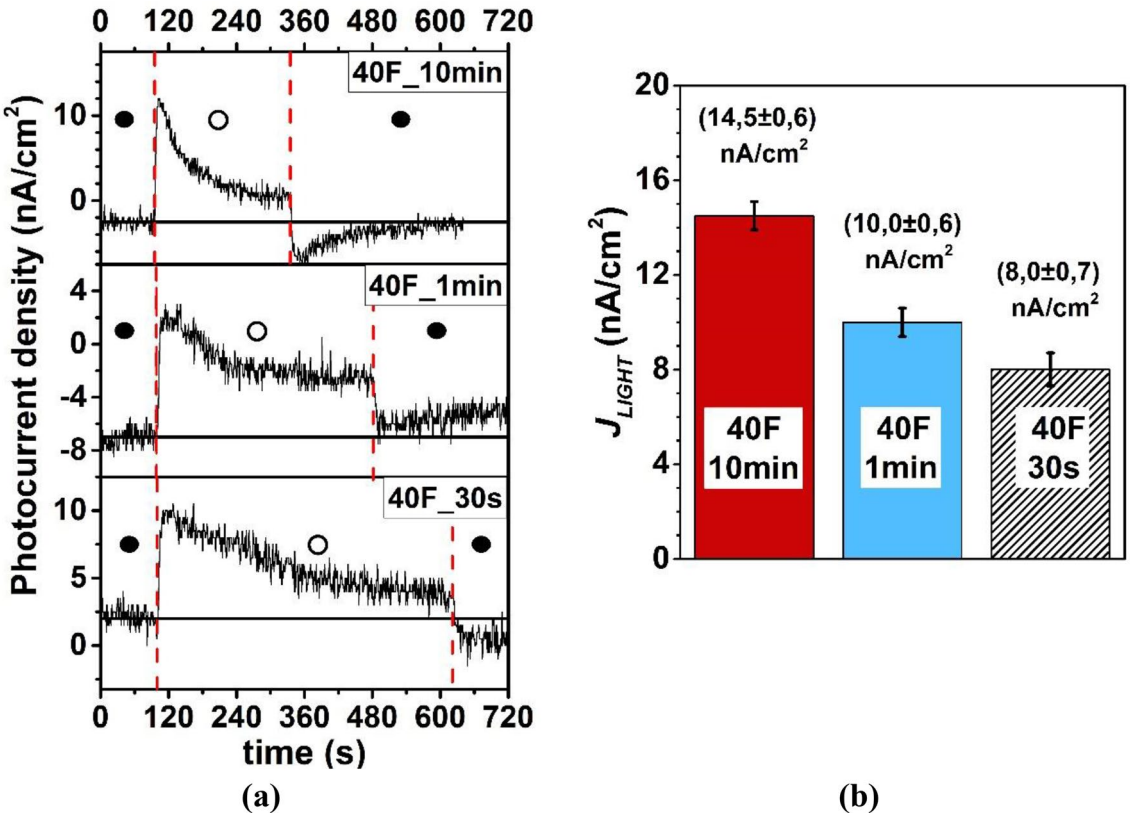

Fig. 4 **a** Time dependence of the short circuit photocurrent density for the three types of photoelectrodes. Filtered white light was used (intensity 200 mW/cm^2 and $\lambda \geq 520$ nm). The white and black circles identify light-on and light-off time intervals, respectively. **b** The column bars show that the difference between the initial dark current and the maximum value reached when light is turned on, J_{LIGHT}; which decreases for shorter immersion times

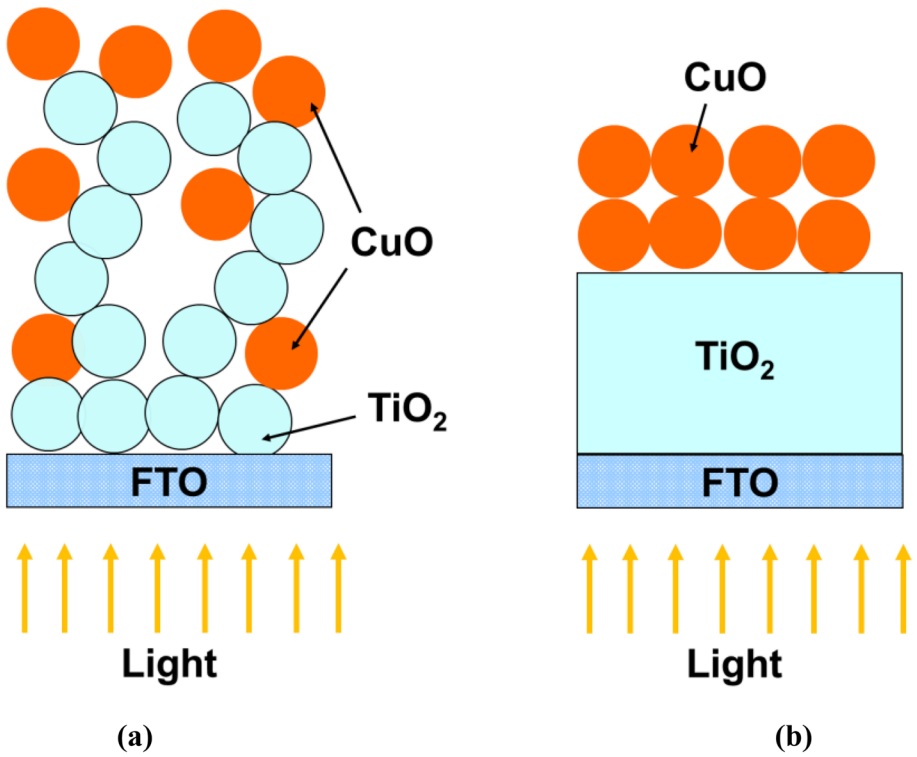

Fig. 5 **a** Diagram of the CuO/TiO_2 nanostructured composite. The dark and light circles correspond to CuO and TiO_2 nanoparticles, respectively. **b** Diagram illustrating the concept of equivalent CuO thickness. It is assumed that light absorbed by CuO/TiO_2 films in the spectral zone where neither the TiO_2 nor the FTO absorb, is equal to that absorbed by a layer of CuO with an equivalent thickness t_{eq}

$$t_{eq} = \frac{\alpha_{com}(\lambda)}{\alpha_{CuO}(\lambda)} \times t_{com} \quad (6)$$

In order to obtain t_{eq}, experimental values of $\alpha_{com}(\lambda)$ (see Fig. 6a) and t_{com} (see Table 1) were used. The spectral dependence of $\alpha_{CuO}(\lambda)$ was obtained from data reported in reference [57].

In Fig. 6a, values of α_{com} vs photon energy are shown for all three films. They were obtained using expression (5) and the experimental reflection and transmittance spectra. Band gap values were obtained from Tauc's expression (7), with $n = 2$ for direct gap [58].

$$\alpha = \frac{A^*}{h\nu}\left(h\nu - E_g\right)^n \quad (7)$$

Figure 6b shows Tauc's plot to find bandgap value for samples 40F_30 s and 40F_1min, $E_g = 1.49 \pm 0.03$ eV and

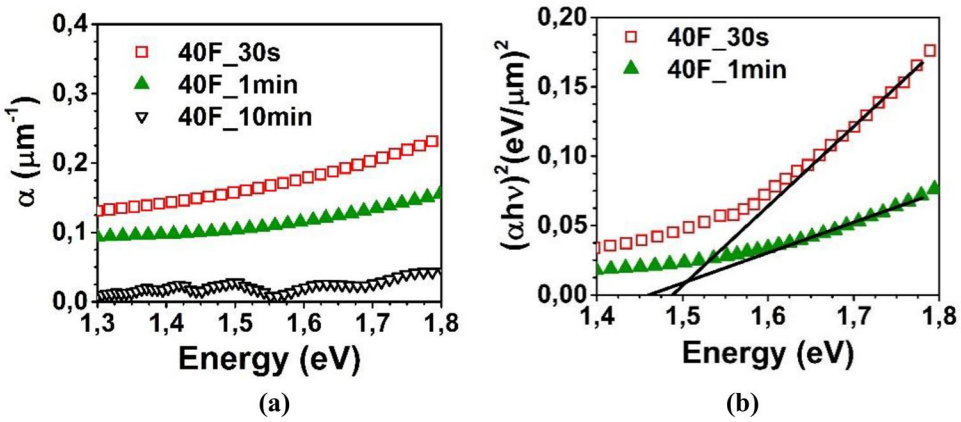

Fig. 6 **a** Absorption coefficient of the samples synthesized using immersion times of 30 s, 1 min and 10 min, and **b** Tauc's dependence to estimate bandgap value

Table 1 Photocurrents comparison for equal optical absorption

Sample	Gap (eV)	J_{LIGHT}(nA/cm^2)	Composite thickness t_{com} (μm)	Equivalent thickness t_{eq} (μm)	Absorbed fraction, F	J_c for equal absorption (nA/cm^2)
40F_30s	1.49 ± 0.03	8.0 ± 0.7	0.5 ± 0.2	0.049 ± 0.001	0.11 ± 0.02	21 ± 2
40F_1min	1.46 ± 0.03	10.0 ± 0.6	1.6 ± 0.3	0.112 ± 0.005	0.23 ± 0.05	12.2 ± 0.7
40F_10 min	1.47 ± 0.06	14.5 ± 0.6	3.0 ± 0.2	0.143 ± 0.003	0.28 ± 0.03	14.5 ± 0.6

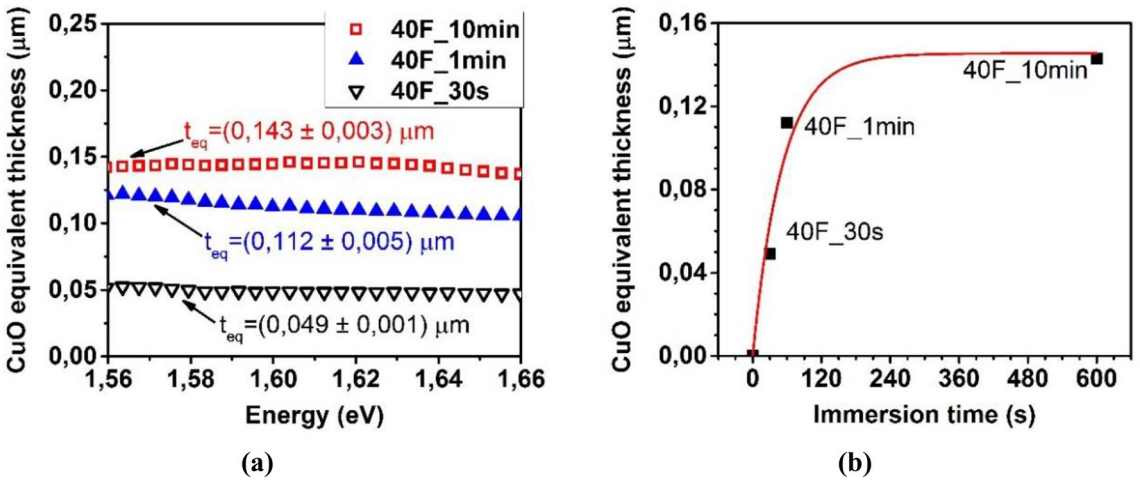

Fig. 7 **a** CuO equivalent thickness of CuO/TiO_2 composites for different immersion time and 40 mM Cu (II) formate as precursor. **b** Inmersion time dependence of CuO equivalent thickness when using 40 mM Cu (II) formate as precursor

$E_g = 1.46 \pm 0.03$ eV, respectively. These values are within the range of those reported for nanostructured CuO [25, 31].

Figure 7a shows that t_{eq} values for the same sample but different photon energy, given by expression (6), are practically constant, confirming our assumptions. In order to define a thickness value t_{eq}, the quadratic average of these values has been used, and its value is also shown in Fig. 7a. Figure 7b shows the behavior of the equivalent thickness of CuO as a function of immersion time.

Figure 7a and b show that the CuO equivalent thickness increases 2.3 times from 30 s to 1 min, while it increases only 1.3 times from 1 to 10 min. This suggests that, during the immersion of the TiO_2 film in the 40 mM Cu (II) formate solution, the deposition speed of the salt inside the TiO_2 mesoporous film decreases with the immersion time (the mass of Cu (II) formate deposited inside the pores determines the mass of CuO formed with the thermal treatment). Behavior shown in Fig. 7b was also observed when using the same technique but a different precursor [51].

4.4 Photocurrents comparison

In order to analyze the effect of nanocrystal size decrease, it is necessary to compare photocurrent produced for an equal number of light created electron–hole pairs in all cases. Therefore, photocurrent values are calculated for the same optical absorption in all samples, i.e., as if adsorbed CuO were the same for all three samples. The total absorbed light intensity, A_C, depends on the absorption for each wavelength. Since light is either reflected, absorbed or transmitted, the absorbed intensity for a CuO thickness t_{eq}, at a certain wavelength, $A(\lambda)$, is [59]:

$$A(\lambda) = I_i(\lambda) \times \left(1 - e^{-\alpha_{CuO}(\lambda) t_{eq}}\right) \tag{8}$$

The absorbed fraction, F, of the incident light intensity corresponding to a wavelength range from λ_1 to λ_2 is given by:

$$F = \frac{\int_{\lambda_1}^{\lambda_2} A(\lambda) \mathrm{d}\lambda}{\int_{\lambda_1}^{\lambda_2} I_i(\lambda) \mathrm{d}\lambda} = \frac{\int_{\lambda_1}^{\lambda_2} I_i(\lambda) \times \left(1 - e^{-\alpha_{CuO} t_{eq}}\right) \mathrm{d}\lambda}{\int_{\lambda_1}^{\lambda_2} I_i(\lambda) \mathrm{d}\lambda} \tag{9}$$

The absorbed fraction F was obtained for each photoelectrode using the equivalent thickness, t_{eq}, (see Fig. 7a) and integrating from $\lambda_1 = 520$ nm to λ_2. This value λ_2 is given by the E_g value of each photoelectrode shown in Table 1. Absorbed fraction F is shown in Table 1, as well as, the corrected photocurrent density value J_c; which is calculated assuming that for all photoelectrodes the optical absorption is that of sample 40F_10 min.

In Table 1, the photocurrent J_c highest value corresponds to the sample with the lowest immersion time and highest bandgap value which corresponds to smallest CuO nanocrystal size. A higher J_c value is explained by a better

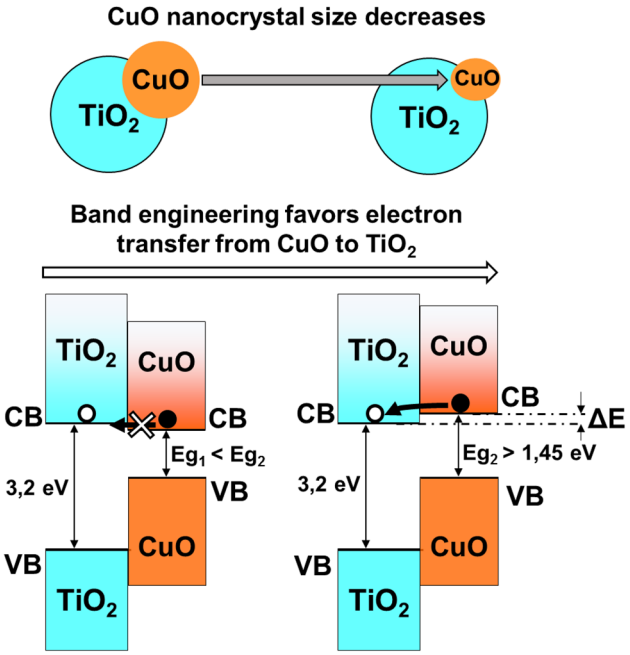

Fig. 8 Changes in bands alignment when nanocrystal size decreases. Black and white circles represent filled and empty states, respectively. Bold arrows indicate electron transfer from the CuO conduction band to the TiO_2. When the difference ΔE between both conduction bands increases because the nanocrystal size decreases, more photoexcited electrons pass to the TiO_2. CB and VB indicate the conduction and valence bands, respectively

alignment of CuO and TiO_2 energy bands that favors electron injection which is caused by a smaller CuO nanocrystal size (see Fig. 8), a correspondingly larger CuO bandgap and a larger difference ΔE between both conduction bands. One can observe in Table 1 a significant difference for calculated photocurrent J_c of sample type 40F_30s. But J_c values are not very different when comparing samples 40F_1min and 40F_10min. This can be explained by nanocrystal size not being very different for the last two samples and being dependent on the amount of CuO deposited shown in Fig. 7b.

J_c values behavior show that it is beneficial to decrease nanocrystal size, even though internal surface area and traps increase. Therefore, passivation of surface defects is recommended together with nanocrystal size decrease.

5 Conclusions

Nanostructured CuO/TiO_2 films have been fabricated using the modified wet-impregnation technique. Used precursor concentration (40 mM Cu (II) formate) and immersion times (10 min, 1 min and 30 s) determine size decrease of deposited CuO nanocrystals. Tauc's analysis of the absorption coefficient spectral dependence indicate bandgap values

of 1.47 ± 0.06 eV, 1.46 ± 0.03 eV and 1.49 ± 0.03 eV for samples 40F_10min, 40F_1min and 40F_30s, respectively. When illuminated with visible light ($\lambda \geq 520$ nm) to prevent photon absorption by TiO_2 and without applied bias, electrons are injected from the CuO to the TiO_2 in all cases; although this is more noticeable for the sample with the smallest nanocrystals and highest bandgap energy. This indicates that when CuO bandgap increases, its conduction band movement to higher energies favors photocurrent increase. Analysis of photocurrent values indicate that it is beneficial to decrease nanocrystal size in spite of internal surface and trap density increase.

Acknowledgements The authors acknowledge the support of the WBI (Fédération Wallonie-Bruxelles) for the financial support through the project SUB/2012/86559

References

1. S. Rühle, A.Y. Anderson, H.N. Barad, B. Kupfer, Y. Bouhadana, E. Rosh-Hodesh, A. Zaban, J. Phys. Chem. Lett. **3**, 3755 (2012)
2. J. Morasch, H.F. Wardenga, W. Jaegermann, A. Klein, Phys. Status Solidi A **213**, 1615 (2016)
3. S.N. Mazhir, H.M. Yaseen, M.M. Salih, G.H. Mohamed, J. Eng. Appl. Sci. **13**, 3555 (2018)
4. F. Wu, Q. Qiao, B. Bahrami, K. Chen, R. Pathak, Y. Tong, X. Li, T. Zhang, R. Jian, Nanotechnology **29**, 215403 (2018)
5. M. Rokhmat, E. Wibowo, Sutisna, Khairurrijal, and M. Abdullah, Procedia Eng. **170**, 72 (2017)
6. M. Rokhmat, E. Wibowo, Sutisna, Khairurrijal, and M. Abdullah, J. Math. Fundam. Sci. **50**, 92 (2018)
7. P. Sawicka-Chudy, G. Wisz, M. Sibiński, Z. Starowicz, Ł. Głowa, M. Szczerba, and M. Cholewa, Optik **206**, 164297 (2020)
8. R. Shashidhar, N. Choudhary, Indian J. Pure Appl. Phys. **58**, 36 (2020)
9. R. Fiorenza, M. Bellardita, S. Scirè, L. Palmisano, Catal. Today **321–322**, 113 (2019)
10. M. I. Maldonado, E. Saggioro, J. Peral, E. Rodríguez-Castellón, J. Jiménez-Jiménez, and S. Malato, Appl. Catal. B Environ. **257**, 117890 (2019)
11. M.W. Kadi, R.M. Mohamed, A.A. Ismail, Ceram. Int. **46**, 8819 (2020)
12. Y. Wang, M. Zhou, Y. He, Z. Zhou, and Z. Sun, J. Alloys Compd. **813**, 152184 (2020)
13. J. Martín-Gómez, J. Hidalgo-Carrillo, R. C. Estévez, F. J. Urbano, and A. Marinas, Appl. Catal. Gen. **620**, 118178 (2021)
14. M. Tripathi, P. Chawla, Int. J. Hydrog. Energy **41**, 7993 (2016)
15. S. Zhang, X.B. Cao, J. Wu, L.W. Zhu, L. Gu, Trans. Nonferrous Met. Soc. China Engl. Ed. **26**, 2094 (2016)
16. J.F. De Brito, F. Tavella, C. Genovese, C. Ampelli, M.V.B. Zanoni, G. Centi, S. Perathoner, Appl. Catal. B Environ. **224**, 136 (2018)
17. S. Rajasekar, V. Tiwari, U. Srivastva, S. Holdcroft, A.C.S. Appl, Energy Mater. **3**, 8988 (2020)
18. S. Jabeen, T.A. Sherazi, R. Ullah, S.A.R. Naqvi, M.A. Rasheed, G. Ali, A.U. Shah, Y. Khan, Appl. Nanosci. Switz. **11**, 79 (2021)
19. W. Srevarit, S. Moonmangmee, P. Phapugrangkul, S. Kuboon, A. Klamchuen, N. Saito, and C. Ponchio, J. Alloys Compd. **859**, 157818 (2021)
20. T.S. Atabaev, D.H. Lee, N.H. Hong, Funct. Mater. Lett. **10**, 1750084 (2017)
21. X. Chen, S.S. Mao, Chem. Rev. **107**, 2891 (2007)
22. Q. Zhang, K. Zhang, D. Xu, G. Yang, H. Huang, F. Nie, C. Liu, S. Yang, Prog. Mater. Sci. **60**, 208 (2014)
23. B. Yan, Y. Wang, T. Jiang, X. Wu, J. Mater. Sci. Mater. Electron. **27**, 5389 (2016)
24. F. Hajakbari and F. Shafieinejad, Jpn. J. Appl. Phys. **55** (2016)
25. B. Sahin, T. Kaya, Microelectron. Eng. **164**, 88 (2016)
26. R.D. Prabu, S. Valanarasu, I. Kulandaisamy, V. Ganesh, M. Shkir, A. Kathalingam, J. Mater. Sci. Mater. Electron. **28**, 6754 (2017)
27. E. Gürbüz and B. Şahin, Appl. Phys. Mater. Sci. Process. **124** (2018)
28. B. Sahin and R. Aydin, Appl. Phys. Mater. Sci. Process. **125** (2019).
29. H. Cavusoglu, R. Aydin, Superlattices Microstruct. **128**, 37 (2019)
30. Ş Baturay, A. Tombak, D. Batibay, Y.S. Ocak, Appl. Surf. Sci. **477**, 91 (2019)
31. T. T. Lun, C. Q. Liu, N. Wang, X. N. Zhai, M. S. Song, Q. Ge, X. Y. Zhang, S. M. Liu, H. L. Wang, W. W. Jiang, and W. Y. Ding, Mater. Lett. **257** (2019)
32. S.F.U. Farhad, S. Majumder, M.A. Hossain, N.I. Tanvir, R. Akter, M.A.M. Patwary, MRS Advances **4**, 937–944 (2019). https://doi.org/10.1557/adv.2019.139
33. E. C. Pastrana, S. J. Loarte, C. D. Gonzales-Lorenzo, R. Y. P. Alta, and H. A. Alarcón, Thin Solid Films **717** (2021)
34. S. A. Al-Shuayfani, A. Loucif, M. Gassoumi, M. N. Shadad, and M. S. Amer, Phys. B Condens. Matter **600** (2021)
35. D. Wang, B. Yan, C. Song, T. Ye, Y. Wang, J. Electron. Mater. **47**, 744 (2018)
36. F. Forcade, R. Snyders, B. González, X. Noirfalise, E. Vigil, Ceram. Int. **44**, 16058 (2018)
37. A. Hagfeldt, M. Graetzel, Chem. Rev. **95**, 49 (1995)
38. T. Soga, in *Nanostructured Mater. Sol. Energy Convers.*, edited by T. Soga (Elsevier, Amsterdam, 2006), pp. 3–43.
39. L. M. Peter, in *Photocatalytic Fundamental Perspective*, edited by J. Schneider, D. Bahnemann, J. Ye, G. L. Puma, and D. D. Dionysiou (Royal Society of Chemistry, 2016), p. 3–28
40. J.S. Curran, D. Lamouche, J. Phys. Chem. **87**, 5405 (1983)
41. W.J. Albery, P.N. Bartlett, J. Electrochem. Soc. **131**, 315 (1984)
42. J. Bisquert, G. Garcia-Belmonte, F. Fabregat-Santiago, J. Solid State Electrochem. **3**, 337 (1999)
43. U. Diebold, Surf. Sci. Rep. **48**, 53 (2003)
44. D. R. Lide, *CRC Handbook of Chemistry and Physics*, 84th ed. (CRC press, 2004).
45. E. Yagi and R. R. Hasiguti, Phys. Rev. B - Condens. Matter Mater. Phys. **54**, 7945 (1996)
46. J.F. Porter, Y.-G. Li, C.K. Chan, J. Mater. Sci. **34**, 1523 (1999)
47. W.Y. Ching, Y.-N. Xu, K.W. Wong, Phys. Rev. B **40**, 7684 (1989)
48. T. Dimopoulos, A. Peić, P. Müllner, M. Neuschitzer, R. Resel, S. Abermann, M. Postl, E. J. W. List, S. Yakunin, W. Heiss, and H. Brückl, J. Renew. Sustain. Energy **5**, 011205 (2013)
49. H. Zheng, J.Z. Ou, M.S. Strano, R.B. Kaner, A. Mitchell, K. Kalantar-Zadeh, Adv. Funct. Mater. **21**, 2175 (2011)
50. S. Rühle, M. Shalom, and A. Zaban, Chem Phys Chem **11**, 2290 (2010).
51. F. Forcade, R. Snyders, G. Guisbiers, B. González, X. Noirfalise, E. Vigil, Mater. Res. Bull. **70**, 248 (2015)
52. E. Vigil, L. Saadoun, R. Rodríguez-Clemente, J. A. Ayllón, and X. Domènech, J. Mater. Sci. Lett. **18**, 1067 (1999)
53. E. Vigil, L. Saadoun, J. A. Ayllón, X. Domènech, I. Zumeta, and R. Rodríguez-Clemente, Thin Solid Films **365**, 12 (2000)
54. I. Zumeta, R. Espinosa, J.A. Ayllón, X. Domènech, R. Rodríguez-Clemente, E. Vigil, Sol. Energy Mater. Sol. Cells **76**, 15 (2003)
55. H. E. Swanson, H. F. Mcmurdie, M. C. Morris, and E. H. Evans, *Standard X-Ray Diffraction Powder Patterns: Data for 81 Substances* (National Bureau of Standards, 1969)
56. S. Asbrink, A. Waskowska, J. Phys. Condens. Matter **3**, 8173 (1991)

57. K. Padrón, E.J. Juárez-Pérez, F. Forcade, R. Snyders, X. Noirfalise, C. Laza, J. Jiménez, E. Vigil, Thin Solid Films **660**, 386 (2018)
58. J. Tauc, R. Grigorovici, A. Vancu, Phys. Status Solidi B **15**, 627 (1966)
59. S. J. Fonash, *Solar Cell Device Physics*, 2nd ed. (Elsevier Inc., 2010)